

Scale and conformal invariance in rotating few-fermion systems

Viktor Bekassy^{1,*} and Johannes Hofmann^{2,3,†}

¹*Department of Microtechnology and Nanoscience (MC2),
Chalmers University of Technology, 41296 Gothenburg, Sweden*

²*Department of Physics, Gothenburg University, 41296 Gothenburg, Sweden*

³*Nordita, Stockholm University and KTH Royal Institute of Technology, 10691 Stockholm, Sweden*

(Dated: October 20, 2023)

We show that rotating two-dimensional Fermi gases possess a nonrelativistic scale and conformal invariance at weak interactions, where the scale invariance of universal short-range interactions is not broken by quantum effects. We demonstrate the symmetry in the excitation spectrum of few-fermion ensembles in a harmonic trap obtained by exact diagonalization, which are constrained by the operator-state correspondence. The excitation spectrum is shown to split in a set of primary states, the energies of which correspond to scaling dimensions of conformal operators, and derived excited states that consist of breathing modes as well as two different center-of-mass excitations, which describe cyclotron and guiding-center excitations of the total particle cloud. Furthermore, the conformal symmetry is manifest in the many-body wave function, where it dictates the form of the hyperradial component, which we demonstrate using Monte Carlo sampling of few-body wave functions.

I. INTRODUCTION

An aim of ultracold quantum gas research is the simulation of strongly correlated phases of matter, in particular to create artificial gauge fields to emulate the physics of the lowest Landau level. In its simplest setting, a synthetic magnetic field is induced in a trapped two-dimensional gas brought in rotation [1–5], which is described in the rotating frame by a substitution [6]

$$H \rightarrow H(\Omega) = H - \Omega L_z, \quad (1)$$

where H is the many-body Hamiltonian of the nonrotating system, Ω is the rotation frequency, and L_z is the out-of-plane angular momentum component. Here, the Hamiltonian H describes nonrelativistic atoms in a harmonic trap with frequency ω that interact with a short-range potential of strength g . The Coriolis force acting on a particle then takes the same form as the Lorentz force on a unit charge in a constant magnetic field of strength $B = 2m^*\Omega$ (m^* is the atomic mass), and an additional centrifugal force weakens the harmonic trap confinement [6]. In the limit in which the rotation frequency approaches the trap frequency, the effective trap potential vanishes and single-particle levels form fully degenerate Landau levels. While such a rapidly rotating gas in the lowest Landau level is seemingly scale invariant due to the complete quenching of the kinetic energy and described by a single Haldane pseudopotential parameter, the noncommutative nature of the guiding center coordinates violates such a scaling symmetry and gives rise to a quantum anomaly [7]. A different quantum anomaly arises if interactions are sufficiently strong to induce transitions between Landau levels: In this case

the contact interaction is renormalized due to virtual excitations, which has been studied extensively in nonrotating systems [8–19]. However, as was shown for these nonrotating systems in a previous work by the present authors [20], virtual excitations only contribute at second order in the interaction strength g , such that the scale symmetry is restored at weak interactions (i.e., to linear order $\mathcal{O}(g)$). In this regime, the scale invariance implies a second symmetry, conformal invariance [21, 22]. Since scale transformations do not affect the angular momentum, we expect that this invariance also holds for rotating systems.

In this work, we confirm that this is indeed the case and rotating 2D Fermi gases at weak interactions are scale and conformally invariant. We use exact diagonalization and many-body degenerate perturbation theory to reveal signatures of scale invariance in the energy spectrum and the statistics of the many-body wave function. A key signature that we establish is that scale and conformal invariance constrain the spectrum of the harmonically trapped rotating gas [22–26], which separates in a set of so-called primary states and their excitations. This is known as the operator-state correspondence, where the energy of primary states is linked to the scaling dimension of conformal operators [27]. The primary states include the ground state and are specific to the particular system. In particular, they depend on the rotation frequency, such that their energy will change compared to the nonrotating gas [20]. From each primary state, we find an infinite set of derived states that are composed of three different excitations: (i) breathing modes, (ii) cyclotron center-of-mass excitations, and (iii) guiding center center-of-mass excitation. The breathing modes are constrained by the conformal symmetry to an excitation energy 2ω of exactly twice the trap frequency, independent of interactions, while the center-of-mass excitations follow from Galilean invariance and have excitation energies $\omega + \Omega$ and $\omega - \Omega$, respectively. The latter two ex-

* bekassy@chalmers.se

† johannes.hofmann@physics.gu.se

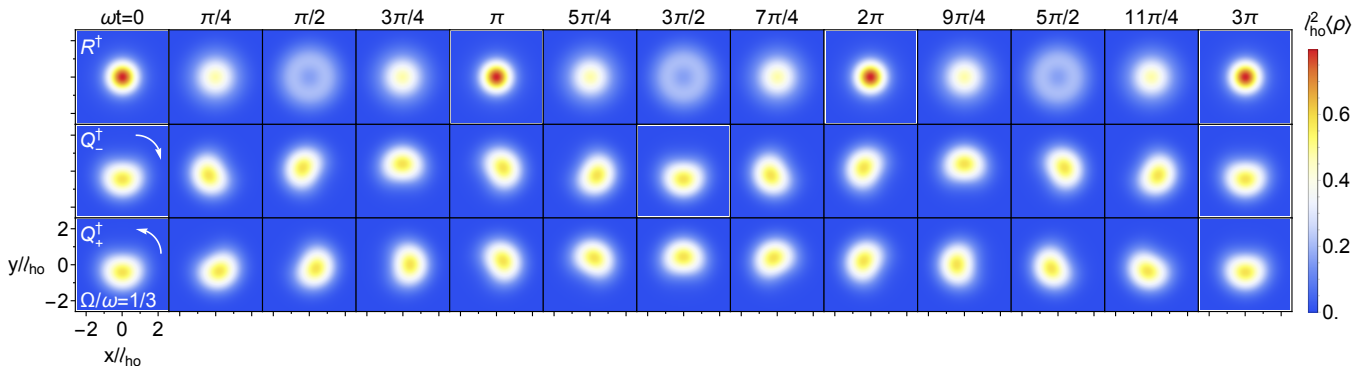


FIG. 1. Time evolution (left to right panels) of the particle density in the stationary frame with rotation frequency $\Omega/\omega = 1/3$ for an equal superposition of the $N = 2$ particle ground state (a primary state) and an excitation by any of the three spectrum-generating operators (top to bottom panels). Top panel: The excitation by R^\dagger induces an undamped internal breathing mode oscillating at exactly twice the trapping frequency, 2ω , independently of both the rotation frequency Ω and interactions. Middle and bottom panels: The center-of-mass excitations Q_-^\dagger and Q_+^\dagger stir the gas in a clockwise or anti-clockwise direction, respectively; the rotation direction is indicated by a white arrow to guide the eye. In contrast to the internal breathing mode excitation, the frequencies of the center-of-mass excitations depend on the rotation, $(\omega + \Omega)$ for Q_-^\dagger , and $(\omega - \Omega)$ for Q_+^\dagger , corresponding to two complete cyclotron cycles in the middle row and one guiding center cycle in the bottom row. White frames indicate the oscillation period.

citations correspond to a cyclotron motion of the center of mass and a drift of the center-of-mass guiding center, respectively. This change in the center-of-mass excitations is a further difference compared to nonrotating systems [20]. Microscopically, the conformal tower structure follows because the Hamiltonian of a rotating trap is part of a symmetry algebra (specifically, the trap potential is at the same time the generator of special conformal transformations [28, 29]). From the symmetry algebra, excitation operators can be created, which we denote by R^\dagger , Q_+^\dagger , and Q_-^\dagger throughout the paper.

To illustrate the nature and naming of these excitations, we show in Fig. 1 density plots in the stationary two-dimensional plane of an equal superposition $|\Psi_0(t)\rangle + |\Psi_e(t)\rangle$ of a ground state wave function $|\Psi_0\rangle$ and the first excited breathing and center-of-mass states $|\Psi_e\rangle = R^\dagger|\Psi_0\rangle$, $Q_-^\dagger|\Psi_0\rangle$, or $Q_+^\dagger|\Psi_0\rangle$, respectively (top to bottom). These wave functions are obtained using the calculations in this paper for $N = 2$ weakly interacting particles in a harmonic trap that rotates at a third of the trap frequency, $\Omega/\omega = 1/3$. The density of a superposition of eigenstates with different energies evolves in time, and horizontal panels show the density plot at time increments $\Delta t = \pi/(4\omega)$ up to one-and-a-half trap periods $T = 2\pi/\omega$. The top panel shows a breathing mode excitation, and indeed the gas is seen to radially expand and contract. As is apparent from the figure, the mode is undamped and completes three cycles in the time period, corresponding to an oscillation frequency of 2ω . [We mark the oscillation period by white frames in Fig. 1 to guide the eye.] The middle panel shows an undamped center-of-mass oscillation—i.e., the atomic cloud moves without any internal deformation—which is seen to complete two full periods in clockwise direction at an increased frequency $\omega + \Omega = 4\omega/3$; this

is the analog of classical cyclotron motion. The bottom panel shows a second undamped center-of-mass excitation, which rotates in counter-clockwise direction with reduced frequency $\omega - \Omega = 2\omega/3$, completing one full rotation, and which is the analog of classical guiding center motion.

In combination, starting from any primary state $|P\rangle$ with energy E_g and angular momentum M_g , an infinite set of breathing and center-of-mass excitations is obtained. We illustrate this conformal tower struc-

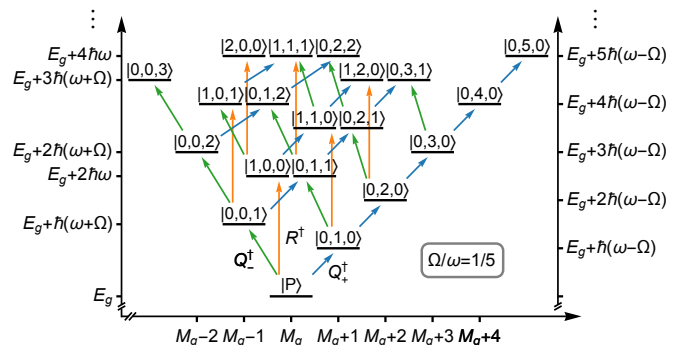


FIG. 2. The conformal tower showing the first nonprimary states derived from a primary state $|P\rangle$ with energy E_g and total angular momentum M_g , shown here for a rotation frequency $\Omega/\omega = 1/5$. Blue arrows are center-of-mass excitations created by Q_+^\dagger that increase the energy by $\hbar(\omega - \Omega)$ and the angular momentum by $+1$, i.e., that stir in the direction of rotation (see Fig. 1). Green arrows are center-of-mass excitations created with Q_-^\dagger that increase the energy by $\hbar(\omega + \Omega)$ and decrease the angular momentum by -1 . Orange arrows are internal breathing modes created by R^\dagger that increase the energy by $2\hbar\omega$ while preserving the angular momentum.

ture in Fig. 2 (here explicitly for a rotation frequency $\Omega/\omega = 1/5$), where the horizontal axis shows the angular momentum and the vertical axis the excitation energy. Vertical orange arrows denote breathing mode excitations, which do not change the angular momentum; green arrows cyclotron center-of-mass excitations, which reduce the total angular momentum; and blue arrows guiding center center-of-mass excitations, which increase the total angular momentum. Every state thus has an associated primary state, which forms the bottom of a conformal tower, and is specified by the number $|a, b, c\rangle$ of breathing and center-of-mass excitations (note that since the excitations are independent, the order in which they are excited is not important). The conjecture is then that for the full excitation spectrum of the weakly interacting rotating gas, we can identify the primary states and all derived excitations in the conformal tower. Indeed, in this paper we confirm the conformal tower structure in the energy spectrum for few-particle ensembles. In addition, we compute and confirm the hyperradial distribution of the many-body wave function using Metropolis importance sampling. We consider few-fermion ensembles of two-component Fermi gases, and our predictions should be observable in experiments on interacting few-body 2D Fermi systems with recently developed single-particle imaging techniques [30–33].

This paper is structured as follows: Section II discusses the level structure of two-component Fermi gases in a rotating harmonic trap and introduces degenerate perturbation theory. Section III then discusses the spectrum generating conformal symmetry algebra that gives rise to the conformal tower structure shown in Fig. 2. These predictions for the level structure are then explicitly verified in our numerical calculations presented in Sec. IV. Additional predictions for the hyperradial part of the many-body wave function are confirmed using Monte Carlo sampling of our eigenstates that are presented in Sec. V. The paper contains two appendices with a derivation of the center-of-mass and the hyperradial wave functions starting from the operator algebra as well as details of the Monte Carlo sampling.

II. PROPERTIES OF ROTATING 2D FERMI GASES

In this work, we reveal the conformal symmetry in the excitation spectrum and many-body wave function for few-fermion ensembles in a rotating harmonic trap with weak contact interactions. This section sets the groundwork for these calculations and discusses the basics of the level structure of rotating Fermi gases, both for free fermions and for contact interactions, and introduces degenerate perturbation theory for weak interactions.

Throughout the paper, we consider two-component fermions with spin projection $\sigma = \uparrow, \downarrow$ and mass m^* (we include an asterisk to avoid possible confusion with an angular momentum quantum number) that are confined

in a two-dimensional harmonic trap with oscillator frequency ω and rotation frequency Ω . We consider fixed-particle number states with $N = N_\uparrow + N_\downarrow$ atoms that contain an equal number of both spin types. We use dimensionless units where both the oscillator energy $\hbar\omega = 1$ and the oscillator length $\ell_{\text{ho}} = \sqrt{\hbar/m^*\omega} = 1$ are set to unity (in particular, the rotation frequency is measured in units of ω). We restore full units in the plots for clarity.

A. Noninteracting rotating Fermi gas

The noninteracting dimensionless Hamiltonian in a harmonic rotating trap in the stationary frame is

$$H^{(0)}(\Omega) = \sum_{j\sigma} \left(-\frac{1}{2} \nabla_{j\sigma}^2 + \frac{r_{j\sigma}^2}{2} + \Omega i \frac{\partial}{\partial \varphi_{j\sigma}} \right), \quad (2)$$

where $r_{j\sigma}$ and $\varphi_{j\sigma}$ label the position of particle j in polar coordinates. The first term is the kinetic energy, the second term describes the harmonic trap potential, and the last term is the out-of-plane-component of the angular momentum operator. The Hamiltonian may be rewritten with a vector potential $\mathbf{A} = m^* \mathbf{e}_z \times \Omega \mathbf{r}$, which describes a unit charged particle in a constant perpendicular magnetic field of strength $\mathbf{B} = 2m^* \Omega$, indicating the mathematical equivalence of the magnetic Lorentz force on a charged particle and the Coriolis force [6]. In addition, after separating the vector potential, the particle experiences a reduced trapping potential $1 - \Omega^2$, such that $\Omega \leq 1$ must hold to ensure that the spectrum is bounded, or physically, that the centrifugal force does not overcome the trapping force.

Single-particle eigenstates of the Hamiltonian (2) are described by two quantum numbers $j = \{n_j, k_j\}$ with $n_j, k_j \geq 0$ and a harmonic oscillator wave function [6]

$$\phi_j(z, \bar{z}) = \sqrt{\frac{\min(n_j, k_j)!}{\pi \max(n_j, k_j)!}} z^{k_j - n_j} e^{-\frac{\bar{z}z}{2}} L_{\min(n_j, k_j)}^{|k_j - n_j|}(\bar{z}z), \quad (3)$$

where $L_{\min(n_j, k_j)}^{|k_j - n_j|}$ is an associated Laguerre polynomial and we use complex coordinates $z = r e^{i\varphi}$. These states are eigenstates of the angular momentum operator with eigenvalue $m_j = k_j - n_j \geq -n_j$. The corresponding eigenenergies are

$$\epsilon_j = 1 + (1 + \Omega)n_j + (1 - \Omega)k_j. \quad (4)$$

Without rotation ($\Omega = 0$), this is the spectrum of the two-dimensional harmonic oscillator, where energy levels with energy $\ell + 1$ are $\ell + 1$ -fold degenerate with degenerate states distinguished by their angular momentum projection $m_j = -\ell, -\ell + 2, \dots, \ell$ (corresponding to $n_j = 0, 1, \dots, \ell$). This is illustrated in Fig. 3(a), where states with $n_j = 0, 1, 2$ are marked in blue, red, and

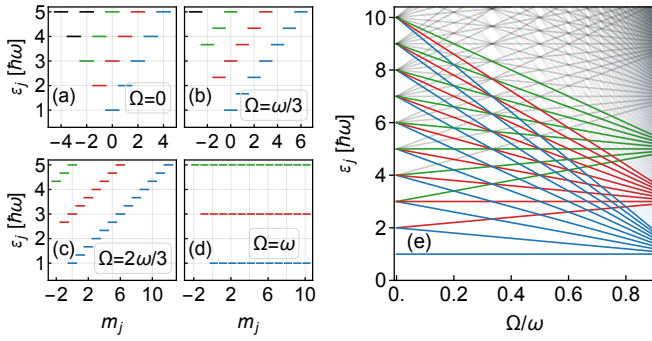


FIG. 3. (a)-(d) Single-particle spectrum of particles in a rotating trap ordered by angular momentum for four different rotation frequencies $\Omega/\omega = 0, 1/3, 2/3$, and 1. States with quantum number $n_j = 0, 1, 2$ are highlighted in blue, red, and green, respectively. In (d), the single-particle energy states form Landau levels. (e) Evolution of the single-particle spectrum as a function of rotation frequency Ω .

green, respectively. In a rotating trap [cf. Figs. 3(b) and (c) for two rotation frequencies $\Omega = 1/3$ and $2/3$], the single-particle levels shift by an amount set by their angular momentum: For angular momenta along the direction of rotation (positive m_j), the energy decreases by $m_j\Omega$; for negative angular momenta, the energy increases by the same amount. As is apparent from the figures, new level degeneracies arise with changing rotation frequency. Finally, in the limit $\Omega \rightarrow 1^-$ where the fermions are no longer trapped [Fig. 3(d)], states with fixed n_j form degenerate Landau levels that are separated by 2Ω . The full evolution of the single-particle spectrum (without resolving the angular momentum) is illustrated in Fig. 3(e), where new degeneracies are visible at rational fractions $\Omega = p/q$ with $p, q \in \mathbb{N}$.

A noninteracting few-particle eigenstate $|\Phi\rangle$ is described by a set of occupied single-particle levels $\{\lambda_1, \lambda_2, \dots\}$, where each level accommodates at most one particle of each spin type [34]. In a position-space projection, these states are represented as a Slater determinant of the single-particle wave functions in Eq. (3) as [35–38]

$$\langle \mathbf{r}_{1\uparrow}, \dots, \mathbf{r}_{1\downarrow}, \dots | \Phi \rangle = \Phi_{\uparrow}(\mathbf{r}_{1\uparrow}, \dots) \cdot \Phi_{\downarrow}(\mathbf{r}_{1\downarrow}, \dots) \quad (5)$$

with

$$\begin{aligned} & \Phi_{\sigma}(\mathbf{r}_{1\sigma}, \dots, \mathbf{r}_{N_{\sigma}\sigma}) \\ &= \frac{1}{\sqrt{N_{\sigma}!}} \begin{vmatrix} \phi_{\lambda_1}(\mathbf{r}_{1\sigma}) & \cdots & \phi_{\lambda_{N_{\sigma}}}(\mathbf{r}_{1\sigma}) \\ \vdots & \ddots & \vdots \\ \phi_{\lambda_1}(\mathbf{r}_{N_{\sigma}\sigma}) & \cdots & \phi_{\lambda_{N_{\sigma}}}(\mathbf{r}_{N_{\sigma}\sigma}) \end{vmatrix}. \end{aligned} \quad (6)$$

Such basis states are odd under any exchange of the N_{\uparrow} positions $\{\mathbf{r}_{1\uparrow}, \dots\}$ or the N_{\downarrow} positions $\{\mathbf{r}_{1\downarrow}, \dots\}$, reflecting the Pauli principle. Energy eigenstates in a rotating isotropic trap are also simultaneous total angular mo-

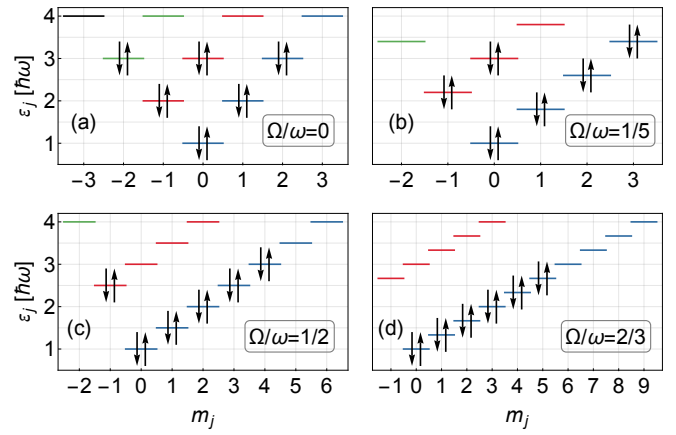


FIG. 4. (a) Ground state of $N = 12$ particles in a nonrotating trap. (b)-(d) Threshold rotation frequencies at which the ground state rearranges to a state with larger total angular momentum. The color coding is the same as in Fig. 3.

mentum eigenstates with

$$M = \sum_{j=1}^{N_{\uparrow}} m_{\lambda_j} + \sum_{j=1}^{N_{\downarrow}} m_{\lambda_j}, \quad (7)$$

which is the sum of the angular momentum projections of occupied single-particle states.

The ground state configuration at a given rotation frequency is obtained by successively populating the lowest single-particle levels with both spins. States obtained in this way are degenerate unless all states at the valence level (the occupied level with highest single-particle energy) are fully occupied. Without rotation, such nondegenerate ground states exist for the “magic” numbers $N = 2, 6, 12, 20, 30, 42, \dots$ with completely filled shells (cf. Fig. 4(a) for the case $N = 12$) [39]. As Ω increases and the single-particle spectrum changes, new degeneracies emerge and the ground state will change in favor of a state with higher total angular momentum. To illustrate this, we show in Figs. 4(b)-(d) the ground state occupancy at the threshold frequencies $\Omega = 1/5, 1/2$, and $2/3$, where the state is degenerate with states with smaller total angular momentum.

Excited states with a given fermion number transfer single fermions or pairs from occupied levels to higher single-particle states. Note that, in general, excited states are highly degenerate even if the ground state is not. To illustrate the degeneracy structure, we show in Fig. 5 the occupancy of the lowest excitation of a $N = 4$ state with rotation frequency $\Omega = 1/3$. The four excited states have degenerate excitation energy $2/3$. While the number of degenerate states is small in this example, it generally grows very quickly both with particle number and excitation energy. For example, excited states with excitation energy 2 for $N = 12$ particles with $\Omega = 0$ are 226-fold degenerate, and for $N = 20$ particles with $\Omega = 1/3$ they are 2060-fold degenerate. In our work, we

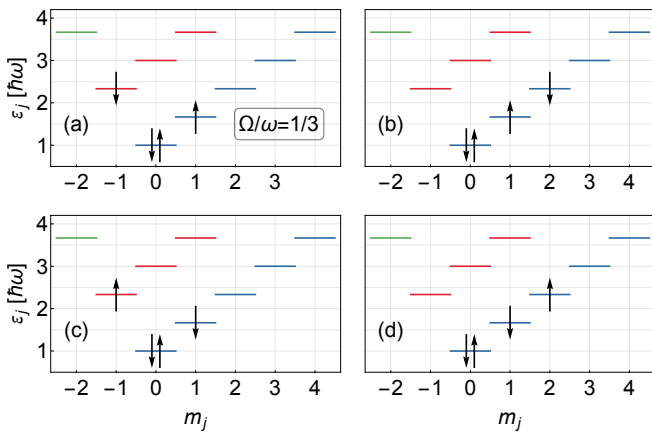


FIG. 5. Four-fold degenerate excited states for the lowest excitation with energy $2\hbar\omega/3$ of the $N=4$ particle ground state with rotation frequency $\Omega/\omega=1/3$. The color coding is the same as in Fig. 3.

identify ground and excited state configurations by numerical counting. We emphasize that the complexity of the subspace of degenerate excited states is still vastly smaller than the size of the full Hilbert space for N particles, at least provided that the trap is not rotating too rapidly.

B. Contact interactions

The ground and excited state degeneracy is lifted when interactions are taken into account. For fermionic quantum gases, these are dominantly short-range s -wave interactions between different spin species that are described in a universal way by a delta function potential

$$H^{(1)} = g \sum_{ij} \delta^{(2)}(\mathbf{r}_{i\uparrow} - \mathbf{r}_{j\downarrow}), \quad (8)$$

with a dimensionless interaction strength g . Since the delta function is a homogeneous function under coordinate rescaling $\delta^{(2)}(\lambda\mathbf{r}) = \lambda^{-2}\delta^{(2)}(\mathbf{r})$, a rescaling of every particle coordinate $\mathbf{r} \rightarrow \lambda\mathbf{r}$ by a constant λ changes the interacting Hamiltonian in the absence of a trapping potential as $H \rightarrow H/\lambda^2$, i.e., the kinetic and the interaction energy transform in the same way and the Hamiltonian is classically scale invariant. However, a delta function interaction in 2D requires renormalization such that the coupling g picks up an additional regulator scale that breaks the scale invariance of the interaction [6], which is known as a quantum scale anomaly [8, 9]. Yet, as argued in [20], we expect that renormalization effects are negligible for weak interactions. The coupling is then indeed scale invariant and given by $g = \sqrt{8\pi}a_{3D}/\ell_z$, with a_{3D} the 3D scattering length and ℓ_z the oscillator length of a transverse harmonic potential [6, 40, 41]. Hence, to linear order in the interaction strength g , the scale invariance of the theory is exact; experimental signatures

of the breaking of scale anomaly enter only at quadratic order [9, 42–45].

We therefore use first-order degenerate perturbation theory in g and restrict our attention to few-particle ensembles to stay in a quasi-2D regime where particles only occupy the lowest state of a transverse harmonic potential. Within first-order degenerate perturbation theory, we collect all states $\{|\Psi_n\rangle\}$ with equal noninteracting energy $E_N^{(0)}$ and diagonalize the Hamiltonian matrix [46, 47]

$$H_{mn} = \langle\Psi_m|H(\Omega)|\Psi_n\rangle \quad (9)$$

to obtain the energy eigenvalues $E_N = E_N^{(0)} + E_N^{(1)}$. Here, $E_N^{(1)} \sim \mathcal{O}(g)$ and scale invariance follow directly from the homogeneity of the delta potential in the matrix element in Eq. (9). By definition of a degenerate subspace, the noninteracting contribution to H_{mn} is a diagonal matrix with equal entries $E_N^{(0)}$, which means that the eigenvectors themselves (unlike the eigenenergies) do not depend on the interaction strength g . Hence, although the eigenvectors we obtain are independent of g , they are still a nontrivial superposition of basis states (5) governed by the nonrelativistic conformal symmetry. Including $\mathcal{O}(g)$ corrections to the eigenvectors corresponds to the next-to-leading order in perturbation theory and involves a divergent summation over all excited states [46, 47], where contributions to eigenenergies are of order $\mathcal{O}(g^2)$. Here, in principle, we anticipate the quantum anomaly to become apparent and the conformal window to close. However, corrections to scale invariance at higher orders can be small [48], and we expect the conformal window to extend beyond the range of validity of leading order perturbation theory.

To evaluate the matrix elements (9), it is convenient to work in an occupation number representation, in which the Hamiltonian (1) takes the form

$$H(\Omega) = \sum_{j,\sigma} \epsilon_j c_{j\sigma}^\dagger c_{j\sigma} + g \sum_{ijkl} w_{ijkl} c_{i\uparrow}^\dagger c_{j\downarrow}^\dagger c_{k\downarrow} c_{l\uparrow}. \quad (10)$$

Here, $c_{j\sigma}^\dagger$ creates a fermion with spin projection $\sigma = \uparrow, \downarrow$ in a single-particle state $j = \{n_j, k_j\}$ with energy ϵ_j given in Eq. (4). The interaction matrix element in Eq. (10) is set by the overlap integral

$$w_{ijkl} = \int d^2r \phi_i^* \phi_j^* \phi_k \phi_l, \quad (11)$$

where ϕ_i is the single-particle wave function in Eq. (3). The overlap integral conserves angular momentum (since $w_{ijkl} \sim \int_0^{2\pi} d\varphi e^{i\varphi(-m_i - m_j + m_k + m_l)}$), making the choice of single-particle eigenstates (3) convenient.

Note that a comprehensive discussion of the ground state properties in a rotating Fermi gas was given by Mashkevich *et al.* [49, 50] in the case of rapid rotations with $\Omega < 1$, i.e., involving occupied Landau level states with $n_j = 0$. Here, the analyticity of the many-body wave function allows for an exact calculation of

the ground state energy even for a general pairwise interaction potential, not just a contact interaction. While excited states within the lowest Landau level can be evaluated in principle using the same method [50], such excitations do not include the breathing mode excitations, which connect different Landau levels, as will be discussed in the next section.

III. PRIMARY STATES AND CONFORMAL TOWERS

In this section, we derive in detail the decomposition of the excitation spectrum into conformal towers composed of primary states and their center-of-mass as well as internal breathing mode excitations, which is illustrated in Fig. 2. The starting point is a spectrum-generating operator implied by the nonrelativistic conformal symmetry [20, 22–26]

$$L^\dagger = iD + H - 2C, \quad (12)$$

where H is the interacting Hamiltonian without rotation, cf. Eq. (1), C is the generator of special conformal transformations $(t, \mathbf{r}) \rightarrow (t, \mathbf{r})/(1 + \lambda t)$, and D is the generator of scale transformations $(t, \mathbf{r}) \rightarrow (t/\lambda^2, \mathbf{r}/\lambda)$. The commutators $[H(\Omega), L^\dagger] = 2L^\dagger$ and $[L_z, L^\dagger] = 0$ imply that when acting on an energy eigenstate, L^\dagger creates an excitation at exactly twice the trapping frequency without any change in the angular momentum. This is also evident in an occupation number representation, where (to leading order in perturbation theory) L^\dagger is a single-particle operator

$$L^\dagger = \sum_{i,j} [2\sqrt{n_i k_i} \delta_{(n_i, k_i), (n_j+1, k_j+1)}] \sum_{\sigma} c_{i\sigma}^\dagger c_{j\sigma} \quad (13)$$

that creates excitations from a state $\{n_j, k_j\}$ to $\{n_j + 1, k_j + 1\}$. Since all operators in Eq. (12) commute with the angular momentum operator, these results continue to hold in a rotating trap. As discussed in the introduction, the excitation is interpreted as an undamped breathing mode excitation. However, it is important to note that the operator L^\dagger mixes internal motion and center-of-mass motion, as we discuss in the following.

A. Center-of-mass excitations

In order to demonstrate and disentangle the mixing of internal and center-of-mass excitations, we introduce two additional independent spectrum-generating operators

$$Q_+^\dagger = \frac{i}{\sqrt{4N}} \left(NZ - 2 \frac{\partial}{\partial \bar{Z}} \right), \quad (14)$$

$$Q_-^\dagger = \frac{i}{\sqrt{4N}} \left(N\bar{Z} - 2 \frac{\partial}{\partial Z} \right), \quad (15)$$

which depend on the center-of-mass coordinate $Z = (1/N) \sum_{i\sigma} z_{i\sigma}$. The center-of-mass excitations generated by Q_\pm^\dagger are illustrated in Fig. 1. These operators have a simple interpretation: They create guiding-center and cyclotron excitations, respectively, for a particle with mass Nm^* in an effective magnetic field $B = 2Nm^*\Omega$ [51]. They obey the commutation relations $[Q_\pm, Q_\pm^\dagger] = 1$, $[H(\Omega), Q_\pm^\dagger] = (1 \mp \Omega)Q_\pm^\dagger$, and $[L_z, Q_\pm^\dagger] = \pm Q_\pm^\dagger$, which implies that Q_+^\dagger creates an excitation with energy $1 - \Omega$ and increases the angular momentum by one unit, and Q_-^\dagger has excitation energy $1 + \Omega$ and decreases the angular momentum, where the change in angular momentum is indicated by the subscript. These results are completely independent of interactions, which only affect internal degrees of freedom. In the limit of fast rotations $\Omega \rightarrow 1^-$, the operator Q_-^\dagger generates the cyclotron resonance between different Landau levels with fixed excitation energy 2Ω [52], while the operator Q_+^\dagger generates gapless excitations that decrease the filling fraction. We expect that in a disk geometry, the latter can be identified with a quasihole excitation [53].

The nature of the center-of-mass excitations also becomes clear in an occupation number representation: The (single-particle) operator Q_-^\dagger creates excitations from an occupied state $\{n_j, k_j\}$ to a state with a higher Landau-level index $\{n_j + 1, k_j\}$,

$$Q_-^\dagger = \frac{1}{\sqrt{2N}} \sum_{i,j} [(-1)^{p_-} i \sqrt{2n_i} \delta_{(n_i, k_i), (n_j+1, k_j)}] \sum_{\sigma} c_{i\sigma}^\dagger c_{j\sigma}, \quad (16)$$

where $p_- = 0$ if $n_i > k_i$ and $p_- = 1$ if $n_i \leq k_i$, whereas Q_+^\dagger excites to levels $\{n_j, k_j + 1\}$ without changing the Landau level

$$Q_+^\dagger = \frac{1}{\sqrt{2N}} \sum_{i,j} [(-1)^{p_+} i \sqrt{2k_i} \delta_{(n_i, k_i), (n_j, k_j+1)}] \sum_{\sigma} c_{i\sigma}^\dagger c_{j\sigma}, \quad (17)$$

where $p_+ = 0$ if $k_i > n_i$ and $p_+ = 1$ if $k_i \leq n_i$.

Returning to the breathing mode excitations, the operators Q_\pm^\dagger and L^\dagger are linearly independent but they do not commute as can be seen from $[L^\dagger, Q_\pm] = -2Q_\mp^\dagger$ and $[L, Q_\pm^\dagger] = 2Q_\mp$. Hence, states generated by L^\dagger and $Q_+^\dagger Q_-^\dagger$ are not orthogonal, which is precisely the statement that a breathing mode generated by L^\dagger also contain center-of-mass excitations. We illustrate this statement in Fig. 6 in the occupation number representation for the simple case of the $N = 2$ ground state $|\text{gs}\rangle$: The operator L^\dagger , Eq. (13), creates an equal superposition of two spin states excited from $\{n_j, k_j\}$ to $\{n_j + 1, k_j + 1\}$, $L^\dagger |\text{gs}\rangle = 2(|\psi_1\rangle + |\psi_2\rangle)$, where the occupation of the states $|\psi_1\rangle$ and $|\psi_2\rangle$ is illustrated in Figs. 6(a) and (b). The center-of-mass excitation generated by the combination $Q_+^\dagger Q_-^\dagger$ create the same superposition with additional two-particle excitations, $Q_+^\dagger Q_-^\dagger |\text{gs}\rangle = \frac{1}{2}(|\psi_1\rangle + |\psi_2\rangle - |\psi_3\rangle - |\psi_4\rangle)$ [Figs. 6(c)

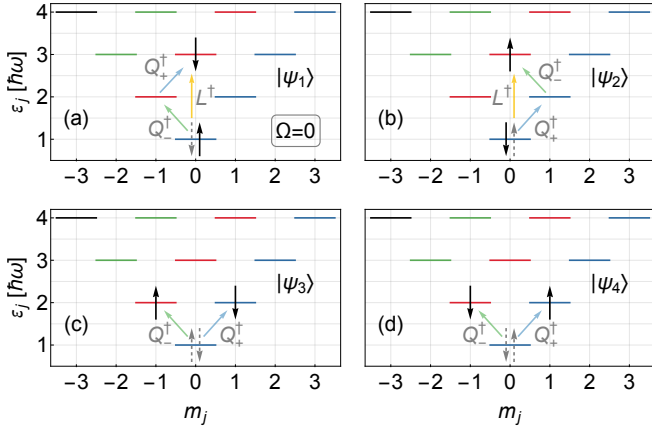


FIG. 6. Occupation number representation of the excited states generated by acting with L^\dagger [(a) and (b)] and $Q_+^\dagger Q_-^\dagger$ [(a)-(d)] on the ground state of $N = 2$ particles without rotation ($\Omega = 0$). Black (gray) spins indicate occupied excited (ground) single-particle states. We denote the action of L^\dagger [Eq. (13)] by a yellow arrow, of Q_-^\dagger [Eq. (16)] by a green arrow, and of Q_+^\dagger [Eq. (17)] by a blue arrow, respectively.

and (d)], which obviously are not orthogonal.

B. Internal breathing mode excitations

We separate the center-of-mass motion from the bare breathing mode excitation by introducing a spectrum-generating operator of *internal* breathing modes

$$R^\dagger = L^\dagger - (Q_+^\dagger Q_-^\dagger + Q_-^\dagger Q_+^\dagger), \quad (18)$$

which commutes with the center-of-mass operators Q_\pm^\dagger . This form of the operator is the same as for a nonrotating trap [20, 25, 26, 54]. Furthermore, it obeys the same commutation relations as L^\dagger , $[H(\Omega), R^\dagger] = 2R^\dagger$ and $[L_z, R^\dagger] = 0$, such that R^\dagger creates an excitation with energy 2 without changing angular momentum. The effect of the operator R^\dagger is to generate the internal breathing mode as illustrated in Fig. 1 in the introduction. It can be shown that R^\dagger acts on the internal hyperradius

$$\tilde{R} = \sqrt{\sum_{i\sigma} |z_{i\sigma} - Z|^2}, \quad (19)$$

which gives the coordinate representation of the internal breathing mode operator

$$R^\dagger = (N - 1) + \tilde{R} \frac{\partial}{\partial \tilde{R}} + s + 1 - \tilde{R}^2, \quad (20)$$

where s parameterizes the energy of a primary state and is defined in the following section in Eq. (26).

In an occupation number representation, states excited by R^\dagger now contain additional two-particle excitations such that they are orthogonal to the center-of-mass

excitation $Q_+^\dagger Q_-^\dagger$. In the example in Fig. 6, we have $R^\dagger|\text{gs}\rangle = |\psi_1\rangle + |\psi_2\rangle + |\psi_3\rangle + |\psi_4\rangle$, which contains the breathing mode excitation $L^\dagger|\text{gs}\rangle$ but is now orthogonal to $Q_+^\dagger Q_-^\dagger|\text{gs}\rangle$. Note that since Q_\pm^\dagger is of order $\mathcal{O}(N^{-1/2})$, the contribution of $Q_+^\dagger Q_-^\dagger$ scales as $\sim 1/N$, and one could naively expect single-particle breathing mode excitations $\{n_j, k_j\}$ to $\{n_j + 1, k_j + 1\}$ to dominate for increasing N . However, there is also an enhancement of order $\mathcal{O}(N)$ of states accessible by two-particle excitations compared to the breathing mode excitations, such that the relative importance of single- and two-particle excitations should thus remain unchanged as N increases. Interestingly, however, the Pauli exclusion principle excludes most two-particle excitations for low-lying energy eigenstates such that R^\dagger is predominantly a single-particle operator for increasing N : In a nonrotating trap, for example, while the $N = 2$ state $R^\dagger|\text{gs}\rangle$ shown in Fig. 6 contains 50% overlap with the breathing mode excitation, this increases to 90% for $N = 6$, to 96% for $N = 12$, and to 98% for $N = 20$. For even higher energy eigenstates and higher breathing mode excitations, two-particle excitations gain importance again.

C. Conformal tower structure

We now discuss the full conformal tower structure shown in Fig. 2. Define a primary state $|P\rangle$ that is annihilated by all spectrum-generating operators R and Q_\pm ,

$$R|P\rangle = Q_+|P\rangle = Q_-|P\rangle = 0. \quad (21)$$

Note that the ground state for any N and Ω is a primary state, but a primary state is not necessarily the ground state: Indeed, there is an infinite number of such states.

A primary state forms the ground step of a conformal tower of orthogonal excited states (the “nonprimary” states) that are created by successively acting on $|P\rangle$ with R^\dagger and Q_\pm^\dagger . We denote these states by

$$|a, b, c\rangle_P = (R^\dagger)^a (Q_+^\dagger)^b (Q_-^\dagger)^c |P\rangle. \quad (22)$$

This is the structure illustrated in Fig. 2, where the energy and angular momentum of a primary state is denoted by E_g and M_g , respectively. Excited states in the figure have energy

$$E_{a,b,c} = E_g + 2a + (1 - \Omega)b + (1 + \Omega)c \quad (23)$$

and angular momentum

$$M_{a,b,c} = M_g + b - c, \quad (24)$$

while the total spin S_N , which defines the eigenvalue $S_N(S_N + 1)$ of the operator

$$S^2 = \sum_{\sigma, \sigma'} \sum_{i, j} \mathbf{S}_{i\sigma} \cdot \mathbf{S}_{j\sigma'}, \quad (25)$$

where $\mathbf{S}_{i\sigma} = \frac{1}{2}\boldsymbol{\sigma}$ is the vector of Pauli matrices, is conserved. The coefficient s that enters the coordinate representation of the internal breathing mode operator in Eq. (20) is defined as

$$E_g = 2 + s - \Omega M_g, \quad (26)$$

and thus sets the ground step energy in a nonrotating trap ($\Omega = 0$). The set of all conformal towers, one for every primary state, forms a complete basis of the Hilbert space.

D. Casimir operator

It is further instructive to discuss the separation of internal and center-of-mass motion on a Hamiltonian level: Introducing internal particle coordinates relative to the center of mass $\tilde{z} = z - Z$, the Hamiltonian splits into an internal part and a center-of-mass part,

$$H(\Omega) = H^{\text{com}}(\Omega) + H^{\text{int}}(\Omega), \quad (27)$$

which always holds for a Galilean invariant interaction. The center-of-mass part describes a fictitious particle of mass Nm^* in a rotating harmonic trap and is expressed solely in terms of the operators Q_{\pm} :

$$H^{\text{com}}(\Omega) = 1 + (1 - \Omega)Q_+^\dagger Q_+ + (1 + \Omega)Q_-^\dagger Q_-, \quad (28)$$

$$L_z^{\text{com}} = Q_+^\dagger Q_+ - Q_-^\dagger Q_-.$$

The decomposition into independent guiding-center and cyclotron excitations of the center of mass is directly visible in this representation. For a given excited nonprimary state, the center-of-mass contribution to the energy and angular momentum are:

$$E_{a,b,c}^{\text{com}} = 1 + (1 - \Omega)b + (1 + \Omega)c, \quad (29)$$

$$M_{a,b,c}^{\text{com}} = b - c.$$

Note that a primary state and its internal breathing mode excitations are completely determined by the relative particle dynamics with internal energy and angular momentum

$$\begin{aligned} E_{a,b,c}^{\text{int}} &= E_g - 1 + 2a, \\ M_{a,b,c}^{\text{int}} &= M_g. \end{aligned} \quad (30)$$

In order to disentangle different primary states and their conformal towers, we introduce the $\text{SO}(2,1)$ Lie Algebra $[T_1, T_2] = -iT_3$, $[T_2, T_3] = iT_1$, and $[T_3, T_1] = iT_2$ with the generators [20]

$$\begin{aligned} T_1 &= \frac{1}{4}(R^\dagger + R), \\ T_2 &= \frac{1}{4i}(R^\dagger - R), \\ T_3 &= \frac{1}{2}(H - H^{\text{com}}) = \frac{1}{2}H^{\text{int}}, \end{aligned} \quad (31)$$

where H^{int} and H^{com} are the internal and center-of-mass parts of the Hamiltonian, respectively, without rotation. This is the algebra of the Lorentz group in 2+1 dimensions, with T_1 and T_2 generating boosts in two directions, and T_3 rotations in the plane [40]. The Casimir operator of the algebra,

$$\begin{aligned} T &= 4(T_3^2 - T_1^2 - T_2^2) \\ &= (H^{\text{int}})^2 - \frac{1}{2}(RR^\dagger + R^\dagger R), \end{aligned} \quad (32)$$

then commutes with the generators in Eq. (31) and is constant within each conformal tower. Its expectation value is

$$\langle T \rangle = \langle a, b, c | T | a, b, c \rangle_P = (s + 1)(s - 1), \quad (33)$$

with s defined in Eq. (26). The value of the Casimir within a conformal tower is thus independent of the rotation frequency.

Following [25, 26], we define a ground step operator $H_g(\Omega)$ by inverting Eq. (32) using $E_{a,b,c}^{\text{int}} = E_g - 1$ for primary states (suppressing the dependence on a, b, c), and $[R, R^\dagger] = 4H^{\text{int}}$, such that

$$H_g(\Omega) = 1 + \sqrt{1 + T} - \Omega L_z^{\text{int}}, \quad (34)$$

where L_z^{int} is the internal angular momentum and both $H_g(\Omega)$ and L_z^{int} are constant within a conformal tower. Evaluating the ground step operator for a state yields the internal energy of the primary state of a conformal tower:

$$\begin{aligned} H_g(\Omega) | a, b, c \rangle_P &= (E_g - 1) | a, b, c \rangle_P \\ &= (1 + s - \Omega M_g) | a, b, c \rangle_P, \end{aligned} \quad (35)$$

where $s = \sqrt{1 + \langle T \rangle}$. One can then define the rescaled internal breathing mode operator

$$r^\dagger = \frac{1}{\sqrt{2}} R^\dagger \left[H^{\text{int}} + H_g(\Omega) + \Omega L_z^{\text{int}} \right]^{-1/2}, \quad (36)$$

where now $[r, r^\dagger] = 1$ [34]. Thus, the total Hamiltonian and the angular momentum $L_z = L_z^{\text{com}} + L_z^{\text{int}}$ is expressed compactly as

$$\begin{aligned} H(\Omega) &= H^{\text{com}}(\Omega) + H_g(\Omega) + 2r^\dagger r, \\ L_z &= Q_+^\dagger Q_+ - Q_-^\dagger Q_- + L_z^{\text{int}}. \end{aligned} \quad (37)$$

In summary, we have established the conformal tower structure in a rotating trap. Compared to a nonrotating trap, the effect of rotations is two-fold: First, it rearranges primary states through the ground step operator $H_g(\Omega)$, and second, it changes the excitation energy of center-of-mass excitations, yet undamped breathing modes at exactly 2ω remain.

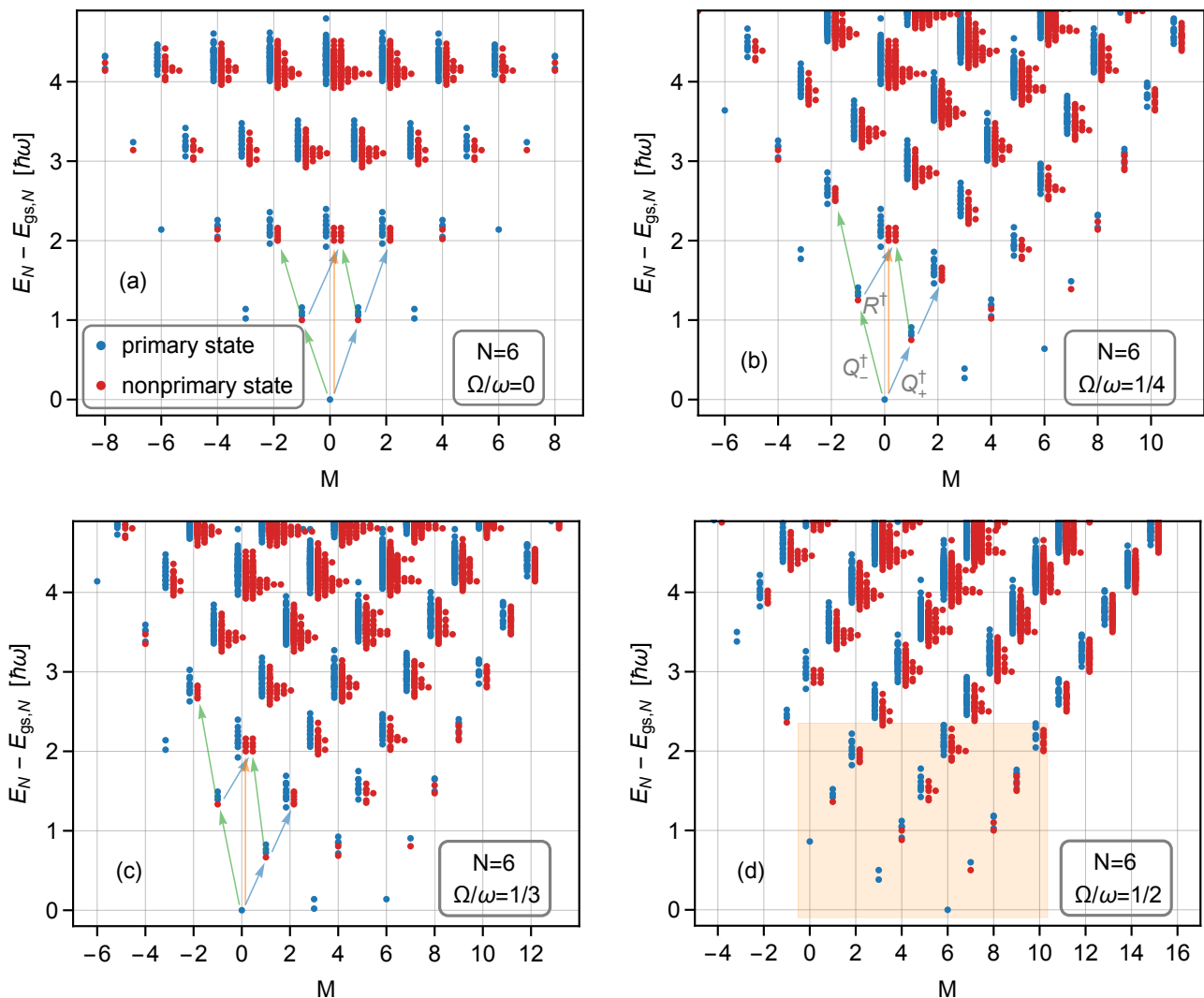


FIG. 7. Excitation energies for $N = 6$ particles in a rotating harmonic trap at rotation frequencies $\Omega/\omega = 0, 1/4, 1/3$ and $1/2$, ordered by angular momentum for an attractive interaction $g = -1$. Primary (nonprimary) states are represented by blue (red) points (cf. Fig. 2) and the color coding is consistent in all plots. Overlapping points are moved horizontally for clarity. In (a)-(c), we indicate by arrows the first few states of the lowest conformal tower originating from the ground state primary state at $M = 0$ (compare with Fig. 2). Each primary blue state sets the ground step for another conformal tower. Orange-colored region: Lowest 115 energy eigenstates for $N = 6$ at $\Omega/\omega = 1/2$ used in Sec. V.

IV. CONFORMAL STRUCTURE IN FEW-FERMION ENSEMBLES

In this section, we explicitly confirm the conformal tower structure outlined in the previous Sec. III by exact diagonalization of the energy spectrum within degenerate first-order perturbation theory. To this end, we construct for a given particle number N the ground and excited state manifolds with equal noninteracting energy $E_N^{(0)}$ and diagonalize the Hamiltonian $H(\Omega)$ [Eq. (10)] as discussed in Sec. II. In the diagonalization, we include the total spin operator S^2 [Eq. (25)], the angular momentum

operator L_z , and the Casimir operator T [Eq. (32)],

$$W = \gamma_1 H(\Omega) + \gamma_2 L_z + \gamma_3 S^2 + \gamma_4 T \quad (38)$$

with incommensurate coefficients $\{\gamma_i\}$. Diagonalizing the matrix W then gives simultaneous eigenstates of all (commuting) operators, and we determine the eigenvalues of the individual operators in Eq. (38) by computing their expectation values with the obtained eigenstates. Primary states and their excited nonprimary states are identified by the first integers (a, b, c) for which an eigenstate is in the kernel of the operators R^{a+1} , Q_+^{b+1} , and Q_-^{c+1} , which connect different degenerate subspaces.

Note that care must be taken when applying this procedure to determine the indices (a, b, c) of the nonpri-

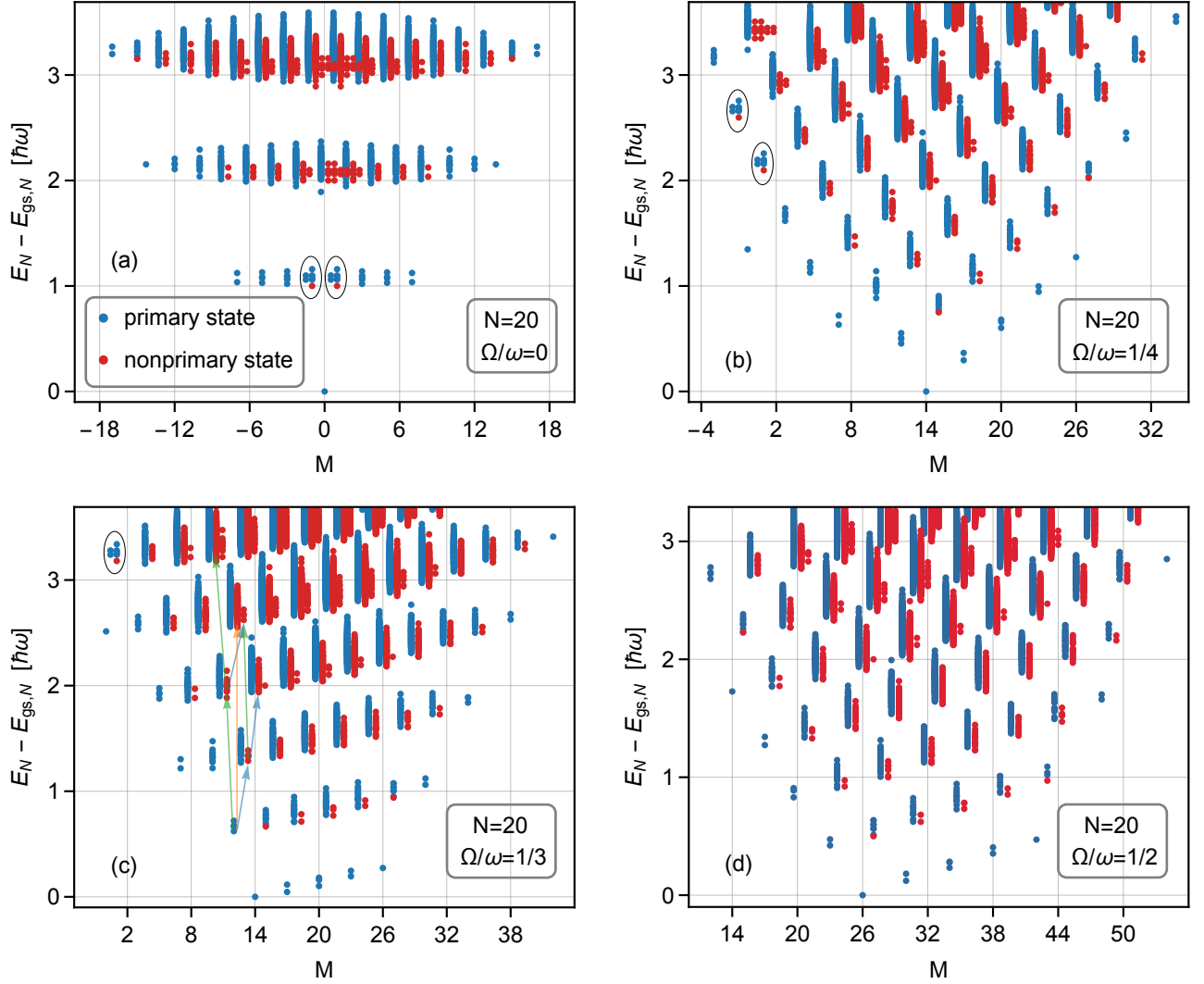


FIG. 8. Excitation energies for $N = 20$ particles in a rotating harmonic trap at rotation frequencies $\Omega/\omega = 0, 1/4, 1/3$ and $1/2$, ordered by angular momentum for an attractive interaction $g = -1$. The color coding is the same as in Fig. 7: Primary states (nonprimary states) are represented by blue (red) points and overlapping points are moved horizontally for clarity. In (c), we indicate by arrows the first few states of the conformal tower originating from an excited primary state at $M = 12$ (compare with Fig. 2). The circled states in panels (a)-(c) show the evolution of a cluster of states under rotations.

primary states, since states $R^\dagger|P\rangle$ and $Q_+^\dagger Q_-^\dagger|P\rangle$ within the same conformal tower share eigenvalues of all operators, cf. Fig. 2 (the same applies to higher breathing mode excitations). Hence, any linear combination $\alpha R^\dagger|P\rangle + \beta Q_+^\dagger Q_-^\dagger|P\rangle$ is a valid eigenstate of (38), independent of the coefficients $\{\gamma_i\}$, and the kernel condition can overcount the indices (a, b, c) for the small subset of such states. To disentangle different nonprimary states, we thus successively apply the diagonalization procedure to degenerate manifolds with increasing excitation energy and store the primary states. Nonprimary states at higher excitation energy are then constructed in a different way by acting on a lower-level primary state with the operators R^\dagger , Q_+^\dagger , and Q_-^\dagger . In all cases, we were able to confirm that these states are identical to the nonprimary

states obtained by explicit diagonalization of (38), which provides a check and confirmation of our analysis, and that for the degenerate subspace with an overcounting of the kernel states they span the same vector subspace.

In Figs. 7 and 8, we show the results for the excitation spectrum obtained from degenerate perturbation theory for particle numbers $N = 6$ [Fig. 7] and 20 [Fig. 8] at four rotation frequencies $\Omega/\omega = 0, 1/4, 1/3$, and $1/2$ (panels (a)-(d)) grouped by angular momentum eigenvalue $M = \langle L_z \rangle$. As discussed, without interactions most states are highly degenerate but interactions lift this degeneracy and split the spectrum, which we visualize using an attractive interaction strength $g = -1$ such that states are still clustered around their noninteracting excitation energies. In the figures, blue points represent

primary states and red points nonprimary states, and we do not indicate different conformal towers for clarity. In addition, we shift primary states to the left and nonprimary states to the right of their angular momentum eigenvalue, and we separate degenerate states horizontally. Note that while the distribution of nonprimary states follows from the nonrelativistic conformal symmetry, the positions of primary states are obtained from our numerical results. The figures show the excitation spectrum with respect to the ground state, which changes as the rotation frequency is increased, cf. the discussion in Sec. II A: For both particle numbers $N = 6$ and $N = 20$, it changes from a zero angular momentum state $M = 0$ to a state with finite angular momentum as the rotation frequency is increased further. For $N = 6$, the finite-angular momentum ground state configuration is of the type shown in Fig. 4(d), where all spins are occupying the lowest possible angular momentum single-particle states with $n_j = 0$. As a consequence, it will remain the ground state for further rotation increase. For $N = 20$, the changing of ground state to $M = 14$ [Fig. 8(b)] corresponds to moving a pair of opposite spins from a single-particle state with $n_j = 3$ to the lowest unoccupied angular momentum single-particle state with $n_j = 0$ and to $M = 26$ [Fig. 8(d)] by moving a pair from $n_j = 0$ and to $M = 26$ [Fig. 8(d)] by moving a pair from $n_j = 2$. As the rotation frequency is increased further, subsequent ground states have angular momentum $M = 42, 54, 70$, and 90.

Comparing different panels in Figs. 7 and 8, the same subclusters are seen in the energy spectrum at different rotation frequencies. Consider, for example, the cluster of states at $M = \pm 1$ around excitation energy 1 in Fig. 8(a) (circled states): As the rotation frequency increases, (b)-(c), the clusters shift in energy but their relative energy within the cluster is unchanged. The same feature is seen for all other clusters at fixed M that are split by the interactions. The reason is that the interaction energy $E_N^{(1)}$ is not affected by rotations to leading order in perturbation theory: Since the overlap integral (11) preserves angular momentum, only states with equal angular momentum have nonzero matrix elements (9). Hence, although states with equal non-interacting energy $E_N^{(0)}$ change due to rotation, states connected by the interaction, i.e., states sharing angular momentum M , are shifted in energy by the same amount $\sim M$, meaning that their relative interaction energy, to leading order perturbation, is independent of rotation.

In all our calculations, we verify the energy spectrum as predicted by the nonrelativistic conformal and Galilean symmetry. For illustration, we indicate by arrows the first few states of the lowest conformal tower in Fig. 7 (a)-(c), where the corresponding primary state is the $N = 6$ particle ground state, which has $M = 0$. The conformal tower structure sketched in Fig. 2 and proven in Sec. III is clearly apparent, with fixed angular-momentum conserving breathing-mode excitations that do not depend on the rotation frequency (vertical ar-

rows in every panel), and center-of-mass excitations that change the angular momentum and that depend on the rotation frequency (diagonal right and left arrows). The analogous conformal tower emanating from the ground primary state is also visible in Fig. 8. Of course, the ground state is not the only primary state, and a plethora of additional primary states emerges in the excitation spectra. For example, in Fig. 7(d) we find 943 primary states out of 3023 total states up to this excitation energy, and in Fig. 8(d) there are 10445 primary states out of 17464 total states shown. For illustration, we indicate the first states in the conformal tower of an excited primary state at $M = 12$ (lowest state in the cluster of primary states) in Fig. 8(c). As discussed, the primary states are unique to the conformal theory and are thus specific to the rotating trapped Fermi gas. The primary eigenvectors themselves are independent of the rotation frequency, but their energy shifts by an amount set by their angular momentum.

V. INTERNAL HYPERRADIAL WAVE FUNCTION

On a microscopic level, the nonrelativistic conformal symmetry has its origin in a factorization of the many-body wave function [25, 26]:

$$\Psi(\mathbf{r}_{1\uparrow}, \dots, \mathbf{r}_{1\downarrow}, \dots) = \Psi_{\text{com}}(Z) \frac{F(\tilde{R})}{\tilde{R}^{N-2}} \phi(\mathbf{n}). \quad (39)$$

Here, $\Psi_{\text{com}}(Z)$ is the center-of-mass part (which factorizes for any Galilean-invariant interaction), $F(\tilde{R})$ is the internal hyperradial part with hyperradius \tilde{R} in Eq. (19), and $\phi(\mathbf{n})$ is a hyperangular part that depends on the remaining internal coordinates $\mathbf{n} = (z_{1\uparrow} - Z, \dots, z_{1\downarrow} - Z, \dots)/\tilde{R}$. We now confirm the hyperradial distribution using the eigenstates determined in the previous section.

The hyperradial distribution $F(\tilde{R})$ is predicted by the conformal symmetry and determined for a state $|a, b, c\rangle_P$ by the condition $(R)^{a+1}|a, b, c\rangle_P = 0$, yielding [20]

$$F(\tilde{R}) = \sqrt{\frac{2a!}{\Gamma(s+a+1)}} \tilde{R}^s e^{-\tilde{R}^2/2} L_a^s(\tilde{R}^2), \quad (40)$$

where Γ is the Gamma function (see App. A for a detailed derivation). The hyperradial wave function depends on the rank of the internal breathing mode excitation a , which sets the number of nodes in the wave function, but it does not depend on center-of-mass parameters b and c since these do not affect the internal dynamics. Furthermore, it depends on the Casimir parameter s [Eq. (33)] that parameterizes the noninteracting energy in the absence of rotations of the corresponding primary state [Eq. (26)]. Thus, states that share the same expectation value of the Casimir operator have the same hyperradial distribution for a given number of breathing mode excitations.

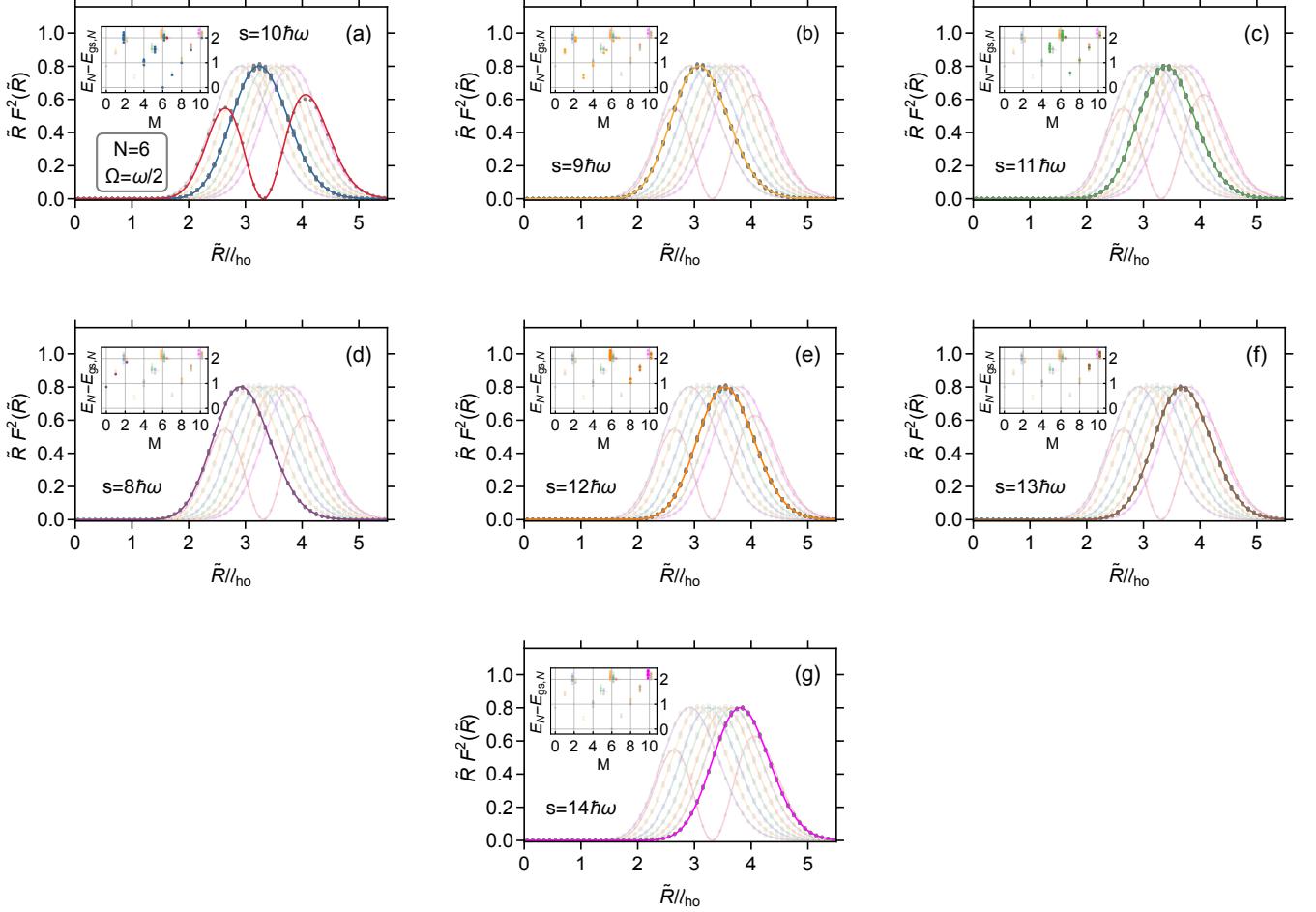


FIG. 9. Distribution of the internal hyperradius \tilde{R} , defined in Eq. (19), for the lowest 115 lowest eigenstates of $N = 6$ particles for $\Omega/\omega = 1/2$. Gray points are the result of a Monte Carlo sampling of the many-body wave function, and continuous lines are the analytical prediction in Eq. (40). Each figure highlights states with a particular value of the Casimir $s = \sqrt{(\hbar\omega)^2 + \langle T \rangle}$ for clarity. The insets show the same energy spectrum as the highlighted region in Fig. 7 but with a color coding that matches the hyperradial distribution.

An experimentally observable consequence of the separability in Eq. (39) is that $\tilde{R}F^2(\tilde{R})$ describes the distribution of the internal hyperradius \tilde{R} , Eq. (19) [26, 55]. We confirm this using Metropolis Monte Carlo sampling of the perturbative wave function $|\Psi_{a,b,c}(\mathbf{r}_{1\uparrow}, \dots, \mathbf{r}_{1\downarrow}, \dots)|^2$ obtained from our diagonalization procedure. Details of the numerical implementation are described in App. B. Figure 9 shows results for the hyperradial distribution computed for the lowest 115 states of $N = 6$ particles with rotation frequency $\Omega = 1/2$ [These states are highlighted in orange in Fig. 7 (d)]. Gray points are Monte Carlo simulations and continuous lines are the analytical predictions in Eq. (40), where the insets show the energy spectrum with a color coding matching the distributions. For clarity, the results for the hyperradial distribution are split into seven figures, where each figure highlights the results of a particular value of s (26) while the rest is opaque to allow a comparison between the figures.

Since multiple states have equal Casimir, Eq. (33), several distributions overlap. For example, Fig. 9(a) shows two distributions with equal value of $s = 10$, where the blue curve is the distribution for 29 different states, and one distribution corresponding to an internal breathing mode excitation of the ground state with $a = 1$. Figures 9(b)-9(g) show one distribution per plot, where all selected states are either primary states with equal s or their center-of-mass excitations [cf. the figure insets]: 16 states in Fig. 9(b), 23 in Fig. 9(c), 3 in Fig. 9(d), 25 in Fig. 9(e), 10 in Fig. 9(f), and 8 in Fig. 9(g). Note that the positions of the peaks in the distributions increases with increasing s , which parameterizes the energy of a primary state without rotation. Hence, in a rotating trap, the most compact distribution [Fig. 9(d)] corresponds to the ground state without rotations and its center-of-mass excitations (i.e., states derived from the primary state in Fig. 9(d) with $M = 0$), even though the former now forms

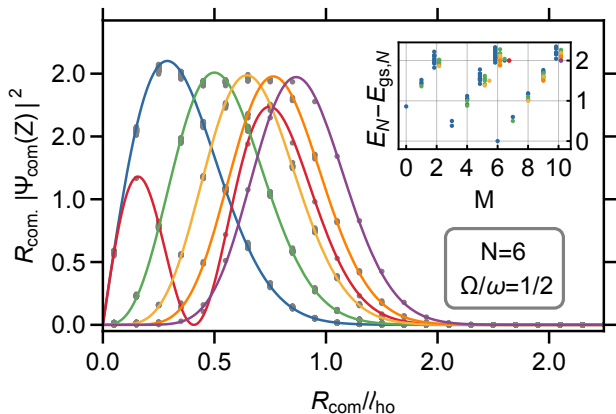


FIG. 10. Distribution of the center-of-mass coordinate $R_{\text{com}} = \sqrt{Z\bar{Z}} = \sqrt{(1/N \sum_{i\sigma} \mathbf{r}_{i\sigma})^2}$ for the lowest 115 eigenstates of $N = 6$ particles for $\Omega/\omega = 1/2$. Gray points are the result of a Monte Carlo sampling of the many-body wave function, and continuous lines are the analytical prediction in Eq. (41). The inset shows the same energy spectrum as the highlighted region in Fig. 7 but with a color coding matching the distribution.

an excited state in the rotating trap.

Different from the hyperradial distribution, the center-of-mass wave function $\Psi_{\text{com}}(Z)$ depends on b and c , and is independent of internal dynamics and thus independent of the interaction potential. The wave function is determined by the relations $(Q_+)^{b+1}|a, b, c\rangle_P = 0$ and $(Q_-)^{c+1}|a, b, c\rangle_P = 0$, yielding for $b \geq c$ (cf. App. A for a derivation)

$$\Psi_{\text{com}}(Z) = \sqrt{\frac{2N^{1+b-c}c!}{b!}} Z^{b-c} e^{-N|Z|^2/2} L_c^{b-c}(N|Z|^2), \quad (41)$$

with Z and \bar{Z} as well as b and c exchanged for $c \geq b$. This is (up to normalization) exactly the wave function of a heavy particle with mass Nm^* in an effective magnetic field $B = 2Nm^*\Omega$ in the c -th Landau level with angular momentum $m = b - c$ [51, 56], again illustrating the interpretation of the center-of-mass modes as guiding-center and cyclotron modes. The center-of-mass wave function (41) neither depends on the energy of the primary state nor the number of breathing mode excitations a . Figure 10 shows the center-of-mass distribution $R_{\text{com}}|\Psi_{\text{com}}(Z)|^2$ as a function of the modulus $R_{\text{com}} = \sqrt{Z\bar{Z}}$, where unlike in Fig. 9 we avoid splitting the plots. As is apparent from the figure, states with the same $\max(b, c)$ and $|b - c|$ share the same center-of-mass distribution. Hence, the distribution for all primary states as well as their internal breathing mode excitations, 64 states in total, collapse onto the blue curve. The red curve with a node corresponds to $b = c = 1$, which describes one out of the 115 lowest states.

The hyperradial distribution (as well as the center-

of-mass distribution) should be observable experimentally, hence verifying the conformal symmetry on a microscopic level, by sampling the many-body wave function with recently developed single-particle imaging techniques [32, 33]. Deviations from our predictions are expected for stronger interactions, corresponding to anomalous symmetry breaking, or deformed traps, corresponding to introducing different length scales and explicitly breaking the symmetry.

VI. CONCLUSION

In this work, we have demonstrated that rotating 2D mesoscopic Fermi gases at weak interactions possess a nonrelativistic conformal symmetry. We confirmed this by means of exact diagonalization of few-fermion ensembles in a harmonic trap, for which the conformal symmetry predicts so-called conformal towers formed by primary states and their center-of-mass and internal breathing mode excitations, the latter having an excitation energy at exactly twice the harmonic trap frequency. From the diagonalization, the eigenstates were used together with Monte Carlo simulations to compute and confirm the hyperradial distribution of the many-body wave function predicted by the symmetry. To the best of our knowledge, this provides the only setup, together with the nonrotating mesoscopic 2D Fermi gas considered in a previous work [20], where the nonrelativistic conformal symmetry can be verified exactly by elementary means in an interacting quantum system. Thus, studying the rotating mesoscopic 2D Fermi gas can not only help our understanding of interacting systems in a magnetic field, but also give new insights into problems such as conformal nonequilibrium dynamics [57–64].

ACKNOWLEDGMENTS

We thank Wilhelm Zwerger for discussions. This work is supported by Vetenskapsrådet (Grant No. 2020-04239) (JH) and the Chalmers' Excellence Initiative Nano under its Excellence Ph.D. program (VB).

Appendix A: DERIVATION OF THE CENTER-OF-MASS AND HYPERRADIAL WAVE FUNCTION

In this appendix we include an operator-based derivation of the center-of-mass wave function in Eq. (41) and the hyperradial distribution in Eq. (40). For the latter, the result is the same as in a nonrotating 3D trap, and an additional derivation can be found in the review by Castin and Werner [26].

1. Center-of-mass wave function

The center-of-mass wave function in Eq. (41) for an excited state $|a, b, c\rangle_P$ follows from the conditions

$$(Q_+)^{b+1}|a, b, c\rangle_P = 0 \quad (\text{A1})$$

$$(Q_-)^{c+1}|a, b, c\rangle_P = 0, \quad (\text{A2})$$

which when written in a coordinate representation [Eqs. (14) and (15)] give two coupled differential equations. Denoting the center-of-mass wave function by $\langle Z, \bar{Z}|a, b, c\rangle_P = \Psi_{b,c}(Z, \bar{Z})$, we begin with the case $b = c = 0$. The first condition (A1) reads:

$$\langle Z, \bar{Z}|Q_+|a, 0, 0\rangle_P \sim \left(2\frac{\partial}{\partial \bar{Z}} + N\bar{Z}\right)\Psi_{0,0}(Z, \bar{Z}) = 0, \quad (\text{A3})$$

which implies $\Psi_{0,0}(Z, \bar{Z}) \sim f(\bar{Z})e^{-\frac{N|\bar{Z}|^2}{2}}$, where $f(\bar{Z})$ is an arbitrary function of the \bar{Z} coordinate. Likewise, inserting $\Psi_{0,0}(Z, \bar{Z})$ in (A2) yields

$$0 = \langle Z, \bar{Z}|Q_-|a, 0, 0\rangle_P \sim \left(2\frac{\partial}{\partial Z} + NZ\right)f(\bar{Z})e^{-\frac{N|\bar{Z}|^2}{2}}, \quad (\text{A4})$$

which implies $f(\bar{Z}) = \text{const}$ and thus an (unnormalized) wave function $\Psi_{0,0}(Z, \bar{Z}) = e^{-\frac{N|\bar{Z}|^2}{2}}$.

The center-of-mass wave function of the excited state $|a, b, 0\rangle_P$ is obtained by acting with $(Q_+^\dagger)^b$ on $\Psi_{0,0}(Z, \bar{Z})$:

$$\begin{aligned} \Psi_{b,0}(Z, \bar{Z}) &= \langle Z, \bar{Z}|(Q_+^\dagger)^b|a, 0, 0\rangle_P \\ &= \left(-2\frac{\partial}{\partial \bar{Z}} + N\bar{Z}\right)^b e^{-\frac{N|\bar{Z}|^2}{2}} \sim Z^b e^{-\frac{N|\bar{Z}|^2}{2}}. \end{aligned} \quad (\text{A5})$$

Assuming $b \geq c$, we determine the general wave function by acting with $(Q_+^\dagger)^c$ on $\Psi_{b,0}(Z, \bar{Z})$:

$$\begin{aligned} \Psi_{b,c}(Z, \bar{Z}) &= \langle Z, \bar{Z}|(Q_+^\dagger)^c|a, b, 0\rangle \\ &= \left(-2\frac{\partial}{\partial \bar{Z}} + N\bar{Z}\right)^c Z^b e^{-\frac{N|\bar{Z}|^2}{2}} \\ &= e^{-\frac{N|\bar{Z}|^2}{2}} Z^{b-c} \sum_{l=0}^c \left(\frac{-N|\bar{z}|^2}{2}\right)^l L_{c-l}^{(b-c)+l} \left(\frac{N|\bar{Z}|^2}{2}\right), \end{aligned} \quad (\text{A6})$$

where in the last line we expanded the prefactor using the binomial formula and used the Rodriguez representation of the associated Laguerre polynomials. Now using the recurrence relation for Laguerre polynomials, we obtain the center-of-mass wave function (for $b \geq c$) stated in Eq. (41) of the main text, which is normalized as $\int d|Z| |Z| |\Psi_{\text{com}}(Z)|^2 = 1$. For $c \geq b$, the derivation is analogous, but with \bar{Z} replacing Z as well as c and b exchanged.

2. Hyperradial Distribution

The hyperradial distribution in Eq. (40) for a state $|a, b, c\rangle_P$ is determined by the relation

$$R^{a+1}|a, b, c\rangle_P = 0. \quad (\text{A7})$$

It is useful to rewrite the R^\dagger operator defined in Eq. (18) as

$$R^\dagger = iD^{\text{int}} + H^{\text{int}} - 2C^{\text{int}}, \quad (\text{A8})$$

with $D^{\text{int}} = -i(N-1) - i\tilde{R}\partial_{\tilde{R}}$ denoting the generator of internal scale transformations, H^{int} the internal Hamiltonian in the absence of rotation ($\Omega = 0$), and $C^{\text{int}} = \tilde{R}^2/2$ the generator of internal special conformal transformations. Acting on a state $|a, b, c\rangle_P$ with H^{int} yields the internal energy in a trap without rotation $s + 1 + 2a$, where $s = \sqrt{1 + \langle T \rangle}$ and T is the Casimir operator in Eq. (32).

Defining

$$\mathcal{F}_{a,s}(\tilde{R}) = \frac{F_{a,s}(\tilde{R})}{\tilde{R}^{N-2}} = \langle \tilde{R}|a, b, c\rangle_P, \quad (\text{A9})$$

the case $a = 0$ follows from

$$\begin{aligned} \langle \tilde{R}|R|0, b, c\rangle_P \\ = \left(- (N-1) - \tilde{R}\frac{\partial}{\partial \tilde{R}} + s + 1 - \tilde{R}^2\right) \mathcal{F}_{0,s}(\tilde{R}) = 0, \end{aligned} \quad (\text{A10})$$

which gives the unnormalized hyperradial distribution $F_{0,s}(\tilde{R}) = \tilde{R}^s e^{-\tilde{R}^2/2} = \tilde{R}^s e^{-\tilde{R}^2/2} L_0^s(\tilde{R}^2)$. The case $a = 1$ is determined by acting with R^\dagger on $|0, b, c\rangle_P$,

$$\begin{aligned} \mathcal{F}_{a,s}(\tilde{R}) &= \left((N-1) + \tilde{R}\frac{\partial}{\partial \tilde{R}} + s + 1 - \tilde{R}^2\right) \frac{F_{0,s}(\tilde{R})}{\tilde{R}^{N-2}} \\ &\sim \tilde{R}^s e^{\tilde{R}^2/2} (s + 1 - \tilde{R}^2) / \tilde{R}^{N-2}, \end{aligned} \quad (\text{A11})$$

which implies $F_{1,s}(\tilde{R}) = \tilde{R}^s e^{\tilde{R}^2/2} (s + 1 - \tilde{R}^2) = \tilde{R}^s e^{\tilde{R}^2/2} L_1^s(\tilde{R}^2)$. Now, the unnormalized form for general a , $F_{a,s}(\tilde{R}) = \tilde{R}^s e^{\tilde{R}^2/2} L_a^s(\tilde{R}^2)$, follows by induction using the internal breathing mode excitation $|a+1, b, c\rangle_P = R^\dagger|a, b, c\rangle_P$. We have:

$$\begin{aligned} \mathcal{F}_{a+1,s}(\tilde{R}) \\ \sim \left((N-1) + \tilde{R}\frac{\partial}{\partial \tilde{R}} + s + 1 + 2a - \tilde{R}^2\right) \mathcal{F}_{a,s}(\tilde{R}) \\ = 2\tilde{R}^{s-N+2} e^{-\frac{\tilde{R}^2}{2}} \left[(s + a + 1 - \tilde{R}^2) L_a^s(\tilde{R}^2) \right. \\ \left. - \tilde{R}^2 L_{a-1}^{s+1}(\tilde{R}^2) \right]. \end{aligned} \quad (\text{A12})$$

Using the recurrence relation for Laguerre polynomials, we end up with

$$F_{a+1,s}(\tilde{R}) \sim \tilde{R}^s e^{-\tilde{R}^2/2} L_{a+1}^s(\tilde{R}^2), \quad (\text{A13})$$

as required. After normalizing $F_{a,s}(\tilde{R})$ according to $\int d\tilde{R} \tilde{R} F_{a,s}^2(\tilde{R}) = 1$, we obtain the hyperradial distribution in Eq. (40) of the main text.

Appendix B: MONTE CARLO SAMPLING OF THE WAVE FUNCTIONS

Having obtained the many-body wave function $\Psi_{a,b,c}(\mathbf{r}_{1\uparrow}, \dots, \mathbf{r}_{1\downarrow}, \dots)$ from the diagonalization of (10), which is a superposition of Slater determinants, we employ Monte Carlo Metropolis sampling of the probability density $|\Psi_{a,b,c}(\mathbf{r}_{1\uparrow}, \dots, \mathbf{r}_{1\downarrow}, \dots)|^2$ (see Ref. [34]). The algorithm is initiated by randomly distributing the particle positions within a radius of ℓ_{ho} around the trap center. We then choose a particle at random and propose a new particle position, $\mathbf{r}'_{j\sigma} = \mathbf{r}_{j\sigma} + \mathbf{r}$, by a distance $r \in [0, \delta]$ with variance $\delta = 0.7\ell_{ho}$, in a random direction, and

compute the ratio

$$\xi = \frac{|\Psi_{a,b,c}(\dots, \mathbf{r}'_{j\sigma}, \dots)|^2}{|\Psi_{a,b,c}(\dots, \mathbf{r}_{j\sigma}, \dots)|^2}. \quad (\text{B1})$$

We accept the new configuration if the ratio $\xi > \xi'$, where $\xi' \in [0, 1]$ is a random number, otherwise we keep the initial configuration. For a given configuration, we compute the center-of-mass coordinate $R_{\text{com}} = \sqrt{(1/N \sum_{i\sigma} \mathbf{r}_{i\sigma})^2}$ and the hyperradius \tilde{R} as defined in Eq. (40) to sample the distribution functions presented in Sec. V. After a warm-up period of 10^4 steps, every new proposed particle configuration is a sampling step, and we build histograms of R_{com} and \tilde{R} with bin size $\Delta R_{\text{com}} = \Delta \tilde{R} = 0.1\ell_{ho}$ for 10^6 sampling steps. The results of this sampling procedure for selected $N = 6$ particle wave functions are shown as gray points in Figs. 9 and 10.

-
- [1] K. W. Madison, F. Chevy, W. Wohlleben, and J. Dalibard, Vortex Formation in a Stirred Bose-Einstein Condensate, *Phys. Rev. Lett.* **84**, 806 (2000).
- [2] J. R. Abo-Shaer, C. Raman, J. M. Vogels, and W. Ketterle, Observation of Vortex Lattices in Bose-Einstein Condensates, *Science* **292**, 476 (2001).
- [3] M. W. Zwierlein, J. R. Abo-Shaer, A. Schirotzek, C. H. Schunck, and W. Ketterle, Vortices and superfluidity in a strongly interacting Fermi gas, *Nature* **435**, 1047 (2005).
- [4] R. J. Fletcher, A. Shaffer, C. C. Wilson, P. B. Patel, Z. Yan, V. Crépel, B. Mukherjee, and M. W. Zwierlein, Geometric squeezing into the lowest Landau level, *Science* **372**, 1318 (2021).
- [5] V. Crépel, R. Yao, B. Mukherjee, R. J. Fletcher, and M. Zwierlein, Geometric squeezing of rotating quantum gases into the lowest Landau level (2023), arXiv:2309.02510.
- [6] I. Bloch, J. Dalibard, and W. Zwerger, Many-body physics with ultracold gases, *Rev. Mod. Phys.* **80**, 885 (2008).
- [7] J. Hofmann and W. Zwerger, Scale Invariance in the Lowest Landau Level, *Comptes Rendus. Physique* **10.5802/crphys.137** (2023).
- [8] M. Olshanii, H. Perrin, and V. Lorent, Example of a Quantum Anomaly in the Physics of Ultracold Gases, *Phys. Rev. Lett.* **105**, 095302 (2010).
- [9] J. Hofmann, Quantum Anomaly, Universal Relations, and Breathing Mode of a Two-Dimensional Fermi Gas, *Phys. Rev. Lett.* **108**, 185303 (2012).
- [10] E. Vogt, M. Feld, B. Fröhlich, S. Pertot, M. Koschorreck, and M. Köhl, Scale Invariance and Viscosity of a Two-Dimensional Fermi Gas, *Phys. Rev. Lett.* **108**, 070404 (2012).
- [11] C. Gao and Z. Yu, Breathing mode of two-dimensional atomic Fermi gases in harmonic traps, *Phys. Rev. A* **86**, 043609 (2012).
- [12] C. Chafin and T. Schäfer, Scale breaking and fluid dynamics in a dilute two-dimensional Fermi gas, *Phys. Rev. A* **88**, 043636 (2013).
- [13] T. Peppler, P. Dyke, M. Zamorano, I. Herrera, S. Hoinka, and C. J. Vale, Quantum Anomaly and 2D-3D Crossover in Strongly Interacting Fermi Gases, *Phys. Rev. Lett.* **121**, 120402 (2018).
- [14] M. Holten, L. Bayha, A. C. Klein, P. A. Murthy, P. M. Preiss, and S. Jochim, Anomalous Breaking of Scale Invariance in a Two-Dimensional Fermi Gas, *Phys. Rev. Lett.* **121**, 120401 (2018).
- [15] J. E. Drut, J. R. McKenney, W. S. Daza, C. L. Lin, and C. R. Ordóñez, Quantum Anomaly and Thermodynamics of One-Dimensional Fermions with Three-Body Interactions, *Phys. Rev. Lett.* **120**, 243002 (2018).
- [16] B. C. Mulkerin, X.-J. Liu, and H. Hu, Collective modes of a two-dimensional Fermi gas at finite temperature, *Phys. Rev. A* **97**, 053612 (2018).
- [17] W. Daza, J. E. Drut, C. Lin, and C. Ordóñez, Virial expansion for the Tan contact and Beth-Uhlenbeck formula from two-dimensional SO(2,1) anomalies, *Phys. Rev. A* **97**, 033630 (2018).
- [18] H. Hu, B. C. Mulkerin, U. Toniolo, L. He, and X.-J. Liu, Reduced Quantum Anomaly in a Quasi-Two-Dimensional Fermi Superfluid: Significance of the Confinement-Induced Effective Range of Interactions, *Phys. Rev. Lett.* **122**, 070401 (2019).
- [19] X. Y. Yin, H. Hu, and X.-J. Liu, Few-Body Perspective of a Quantum Anomaly in Two-Dimensional Fermi Gases, *Phys. Rev. Lett.* **124**, 013401 (2020).
- [20] V. Bekassy and J. Hofmann, Nonrelativistic conformal invariance in mesoscopic two-dimensional Fermi gases, *Phys. Rev. Lett.* **128**, 193401 (2022).
- [21] C. R. Hagen, Scale and Conformal Transformations in Galilean-Covariant Field Theory, *Phys. Rev. D* **5**, 377 (1972).
- [22] W. Zwerger, Basic Concepts and some current Directions in Ultracold Gases, Lectures on many-body phenomena in ultracold gases, Collège de France (2021).
- [23] L. P. Pitaevskii and A. Rosch, Breathing modes and hidden symmetry of trapped atoms in two dimensions, *Phys. Rev. A* **55**, R853 (1997).
- [24] Y. Castin, Exact scaling transform for a unitary quantum gas in a time dependent harmonic potential, *Comptes Rendus Physique* **5**, 407 (2004).

- [25] F. Werner and Y. Castin, Unitary gas in an isotropic harmonic trap: Symmetry properties and applications, *Phys. Rev. A* **74** (2006).
- [26] Y. Castin and F. Werner, The Unitary Gas and its Symmetry Properties, in *The BCS–BEC Crossover and the Unitary Fermi Gas*, edited by W. Zwerger (Springer (Heidelberg), 2012).
- [27] Y. Nishida and D. T. Son, Nonrelativistic conformal field theories, *Phys. Rev. D* **76**, 086004 (2007).
- [28] T. Mehen, I. W. Stewart, and M. B. Wise, Conformal invariance for non-relativistic field theory, *Physics Letters B* **474**, 145 (2000).
- [29] D. T. Son and M. Wingate, General coordinate invariance and conformal invariance in nonrelativistic physics: Unitary Fermi gas, *Annals of Physics* **321**, 197 (2006).
- [30] A. Bergschneider, V. M. Klinkhamer, J. H. Becher, R. Klemt, G. Zürn, P. M. Preiss, and S. Jochim, Spin-resolved single-atom imaging of ${}^6\text{Li}$ in free space, *Phys. Rev. A* **97**, 063613 (2018).
- [31] L. Bayha, M. Holten, R. Klemt, K. Subramanian, J. Bjerrin, S. M. Reimann, G. M. Bruun, P. M. Preiss, and S. Jochim, Observing the emergence of a quantum phase transition shell by shell, *Nature* **587** (2020).
- [32] M. Holten, L. Bayha, K. Subramanian, C. Heintze, P. M. Preiss, and S. Jochim, Observation of Pauli Crystals, *Phys. Rev. Lett.* **126**, 020401 (2021).
- [33] M. Holten, L. Bayha, K. Subramanian, S. Brandstetter, C. Heintze, P. Lunt, P. M. Preiss, and S. Jochim, Observation of Cooper pairs in a mesoscopic two-dimensional Fermi gas, *Nature* **606**, 287 (2022).
- [34] V. Bekassy, *Rotating Two-Dimensional Mesoscopic Fermi Gases and Nonrelativistic Conformal Invariance*, Master's thesis, Chalmers University of Technology (2023).
- [35] J. C. Slater, The theory of complex spectra, *Phys. Rev.* **34**, 1293 (1929).
- [36] J. C. Slater, Molecular energy levels and valence bonds, *Phys. Rev.* **38**, 1109 (1931).
- [37] E. U. Condon, The theory of complex spectra, *Phys. Rev.* **36**, 1121 (1930).
- [38] P.-O. Löwdin, Quantum Theory of Many-Particle Systems. I. Physical Interpretations by Means of Density Matrices, Natural Spin-Orbitals, and Convergence Problems in the Method of Configurational Interaction, *Phys. Rev.* **97**, 1474 (1955).
- [39] F. Resare and J. Hofmann, Few-to-many particle crossover of pair excitations in a superfluid (2022), arXiv:2208.03762.
- [40] W. Zwerger, Strongly Interacting Fermi Gases, in *Proceedings of the International School of Physics "Enrico Fermi" - Course 191 "Quantum Matter at Ultralow Temperatures"*, edited by M. Inguscio, W. Ketterle, S. Stringari, and G. Roati (arXiv:1608.00457, 2016) p. 63.
- [41] J. Hofmann and W. Zwerger, Universal relations for dipolar quantum gases, *Phys. Rev. Research* **3**, 013088 (2021).
- [42] C. Langmack, M. Barth, W. Zwerger, and E. Braaten, Clock Shift in a Strongly Interacting Two-Dimensional Fermi Gas, *Phys. Rev. Lett.* **108**, 060402 (2012).
- [43] J. Hofmann, High-temperature expansion of the viscosity in interacting quantum gases, *Phys. Rev. A* **101**, 013620 (2020).
- [44] T. Enss, Bulk Viscosity and Contact Correlations in Attractive Fermi Gases, *Phys. Rev. Lett.* **123**, 205301 (2019).
- [45] Y. Nishida, Viscosity spectral functions of resonating fermions in the quantum virial expansion, *Annals of Physics* **410**, 167949 (2019).
- [46] J. J. Sakurai, *Modern Quantum Mechanics* (Addison-Wesley (Reading, Massachusetts), 1994).
- [47] K. Gottfried and T.-M. Yan, *Quantum Mechanics: Fundamentals* (Springer (New-York), 2003).
- [48] E. Taylor and M. Randeria, Apparent Low-Energy Scale Invariance in Two-Dimensional Fermi Gases, *Phys. Rev. Lett.* **109**, 135301 (2012).
- [49] S. Mashkevich, S. Matveenko, and S. Ouvry, Exact results for the spectra of bosons and fermions with contact interaction, *Nuclear Physics B* **763**, 431 (2007).
- [50] S. Mashkevich, S. Matveenko, and S. Ouvry, Exact results for the spectra of interacting bosons and fermions on the lowest Landau level (2011), arXiv:1112.2197.
- [51] A. H. MacDonald, Introduction to the Physics of the Quantum Hall Regime (1994), arXiv:cond-mat/9410047.
- [52] W. Kohn, Cyclotron Resonance and de Haas-van Alphen Oscillations of an Interacting Electron Gas, *Phys. Rev.* **123**, 1242 (1961).
- [53] M. Kasner, Electronic correlation in the quantum Hall regime, *Annalen der Physik* **514**, 175 (2002).
- [54] S. Moroz, Scale-invariant Fermi gas in a time-dependent harmonic potential, *Phys. Rev. A* **86**, 011601 (2012).
- [55] D. Blume, J. von Stecher, and C. H. Greene, Universal Properties of a Trapped Two-Component Fermi Gas at Unitarity, *Phys. Rev. Lett.* **99**, 233201 (2007).
- [56] G. F. Giuliani and G. Vignale, *Quantum Theory of the Electron Liquid* (Cambridge University Press (Cambridge), 2005).
- [57] R. Bamler and A. Rosch, Equilibration and approximate conservation laws: Dipole oscillations and perfect drag of ultracold atoms in a harmonic trap, *Phys. Rev. A* **91**, 063604 (2015).
- [58] J. Maki, L.-M. Zhao, and F. Zhou, Nonperturbative dynamical effects in nearly-scale-invariant systems: The action of breaking scale invariance, *Phys. Rev. A* **98**, 013602 (2018).
- [59] J. Maki and F. Zhou, Quantum many-body conformal dynamics: Symmetries, geometry, conformal tower states, and entropy production, *Phys. Rev. A* **100**, 023601 (2019).
- [60] R. Saint-Jalm, P. C. M. Castilho, E. Le Cerf, B. Bakali-Hassani, J.-L. Ville, S. Nascimbene, J. Beugnon, and J. Dalibard, Dynamical Symmetry and Breathers in a Two-Dimensional Bose Gas, *Phys. Rev. X* **9**, 021035 (2019).
- [61] C. Lv, R. Zhang, and Q. Zhou, $SU(1,1)$ Echoes for Breathers in Quantum Gases, *Phys. Rev. Lett.* **125**, 253002 (2020).
- [62] Z.-Y. Shi, C. Gao, and H. Zhai, Ideal-Gas Approach to Hydrodynamics, *Phys. Rev. X* **11**, 041031 (2021).
- [63] M. Olshanii, D. Deshommes, J. Torrents, M. Gonchenko, V. Dunjko, and G. E. Astrakharchik, Triangular Gross-Pitaevskii breathers and Damski-Chandrashkar shock waves, *SciPost Phys.* **10**, 114 (2021).
- [64] J. Maki and F. Zhou, Emergent infrared conformal dynamics in strongly interacting quantum gases (2023), arXiv:2305.19061.